

# Analytical approach to high harmonics spectrum in the nanobunching regime

Mykyta Cherednychek and Alexander Pukhov

*Institut für theoretische Physik, Heinrich-Heine-Universität Düsseldorf*

August 12, 2016

## Abstract

With the high-order harmonic generation (HHG) from plasma surfaces it is possible to turn a laser pulse into a train of attosecond or even zeptosecond pulses in the backward radiation. These attosecond pulses may have amplitude several orders of magnitude higher than that of the laser pulse under appropriate conditions. We study this process in detail, especially the nanobunching of the plasma electron density. We derive an analytical expression that describes the electron density profile and obtain a good agreement with particle-in-cell simulation results. We investigate the most efficient case of HHG at moderate laser intensity ( $I \approx 2 \cdot 10^{20} \text{ W/cm}^2$ ) on the over-dense plasma slab with an exponential profile pre-plasma. Subsequently we calculate the spectra of a single attosecond pulse from the backward radiation using our expression for the density shape in combination with the equation for the spectrum of the nanobunch radiation.

## 1 Introduction

Since the invention of laser in the year of 1960 [1], laser technology has witnessed an immense progress [2–16]. The revolutionary invention of the chirped pulse amplification technique brought the laser to a completely new level [2]. Roughly twenty years later a record peak intensity of order  $10^{22} \text{ W/cm}^2$  was reached by focusing a 45-TW laser beam [12]. Recently, a compression scheme has been proposed that opens the possibility to generate ultra-short and ultra-strong laser pulses with focused intensities of  $10^{24} \text{ W/cm}^2$  and duration of 2fs [16].

This progress offers an opportunity to study new physical phenomena of laser plasma interactions. One of the most important processes in this field is the HHG, which has been studying very intensely nowadays. As the minimum achievable duration of laser pulses continuously reduces towards few femtoseconds, the generation of even shorter pulses (in the attosecond or even zeptosecond range) is possible only for radiation with shorter wavelengths. The reduction of the pulse duration and the radiation wavelength would open new horizons for potential applications. This is the main motivation to study the HHG.

First observations of HHG from plasmas were made in 1981 [17, 18]. Rather matured is HHG in gases that allows to generate single attosecond pulses with

duration less than 1fs [19–22]. However, this method of HHG requires the limitation of laser pulse intensity by maximum  $10^{15} \text{W/cm}^2$  in order to prevent the ionization.

Fortunately, there is another method of efficient production of high order harmonics by unlimited laser power. This is the interaction process of high contrast laser pulses [23] with solid density targets. The pedestal of the pulse ionizes the surface and the main pulse interacts with electrons of the overdense plasma, while ions remain nearly immobile during the short pulse duration. One distinguishes two main HHG mechanisms in this case: coherent wake emission (CWE) [23–25] and the “relativistically oscillating mirror” (ROM) [27–35].

CWE is caused by fast Brunel electrons [26], which excite plasma oscillations at the local plasma frequencies. Thus, there are no harmonics beyond the maximal plasma frequency in the case of CWE. This process dominates for non-relativistic laser intensities  $a_0 \lesssim 1$ . For  $a_0 \gg 1$  the harmonics are generated mostly via the ROM mechanism. In this case, the electron layer at the plasma surface acts as a mirror that oscillates at relativistic velocities, resulting in the generation of high order harmonics via Doppler effect when the surface moves towards the incident wave. During this process there is no limit of frequency like by CWE, so higher harmonics can be generated. The first theoretical description of ROM claimed that the intensity spectrum envelope of reflected wave can be described by  $I(n) \propto n^{-5/2}$  up to the “roll over” frequency  $\omega_r$  which is proportional to  $4\gamma^2$ , where  $n$  is the harmonic order and  $\gamma$  is the relativistic gamma factor [30]. Later this theory was improved, especially the acceleration of the reflecting layer was taken into account. This leads to the power law  $I(n) \propto n^{-8/3}$  and  $\omega_r \propto \gamma^3$  [32]. This model assumes the existence of a so called apparent reflection point (ARP) where the transverse electric field vanishes. Predictions based on that model were experimentally confirmed [33–35].

Most recently another HHG mechanism was discovered. Using p-polarized oblique incident light with  $a_0 \gg 1$  one can cause the formation of extremely dense electron nanobunches under appropriate conditions. These bunches can emit attosecond pulses with intensities much larger compared to the incident pulse [36, 37]. This means that the boundary condition assumed in [32] corresponding to ARP fails and thus the ROM theory can not be applied in this case. This process is called coherent synchrotron emission (CSE). The reflected radiation in case of CSE is characterized by the power law  $I(n) \propto n^{-4/3}$  or  $I(n) \propto n^{-6/5}$  which is flatter comparing to ROM [36, 37]. The corresponding experiments can be found in Ref. [38–40]. Detailed numerical investigation of the case of p-polarized oblique incidence in Ref. [41] demonstrate that the ROM model can be violated when the similarity parameter  $S = n/a_0$  (where  $n$  is the electron density given in units of the critical density  $n_c$  and  $a_0$  is the dimensionless laser amplitude [42]) is smaller than five. The authors of [41] present a new relativistic electronic spring (RES) model for  $S < 5$ .

Since usually one obtains a train of attosecond pulses by HHG, the question is whether it is possible to isolate one single pulse. One method is to use the polarization gate technique [43, 44]. This is important because it opens the opportunity to a number of potential applications [45]. Successful application of  $\lambda^3$  focusing could even lead to investigation of vacuum instabilities [31, 46].

We pursue two main goals in this work. The first one is to provide a more detailed analytical description of the spectrum in the case of CSE compared to [36, 37]. For this purpose we introduce an analytical approach which allows

us to calculate the electron density profile of the given nanobunch as well as its current distribution, that are used in formulas for back-radiating spectrum derived in [36,37]. Subsequently we compare the derived expressions with one-dimensional simulation results done with the VLPL PIC code.

The second aim is to determine the most efficient case of HHG at moderate laser intensity ( $I \approx 2 \cdot 10^{20} \text{ W/cm}^2$ ). For that reason we perform several 1D PIC simulations with different parameters. Finally, we analyze the obtain results and define different regimes of HHG.

In the last section of the paper we consider the nanobunches moving and radiating in forward direction.

## 2 PIC simulation of the HHG process

For our simulations we use the one-dimensional version of the VLPL PIC code [47]. In our geometry, the incident wave comes from the left hand side of the simulation box and propagates along the  $x$ -axis. The wave is p-polarized and the electric field component oscillates along the  $y$ -axis. The plasma is located at the right hand side of simulation box. It is also possible to simulate oblique incidence with our code. Let  $\theta$  be the angle of incidence in the laboratory frame and consider a frame moving along the  $y$ -axis with velocity  $V = c \sin \theta$ . Lorentz transformations verify that the laser is normally incident in this frame. At the same time the whole plasma moves in  $y$ -direction in the frame. Thus, attributing some initial velocity to plasma in our simulation, we are working in the moving frame. If we need to get the results in laboratory frame, we have to transform the values obtained from the simulation via Lorentz transformation. Consequently we obtain results that correspond to the process with oblique incidence. We use the incident wave  $E_i(\tau)$  of duration  $T = 10\lambda/c$ , that is given by

$$E_i(\tau) = \frac{1}{4} \left( 1 + \tanh \left( \frac{\tau}{\Delta t} \right) \right) \left( 1 - \tanh \left( \frac{\tau - T}{\Delta t} \right) \right) \sin(2\pi\tau),$$

where  $\Delta t = \lambda/4$  and  $\tau = t - x/c$  (Fig. 1a). Further we use an exponential

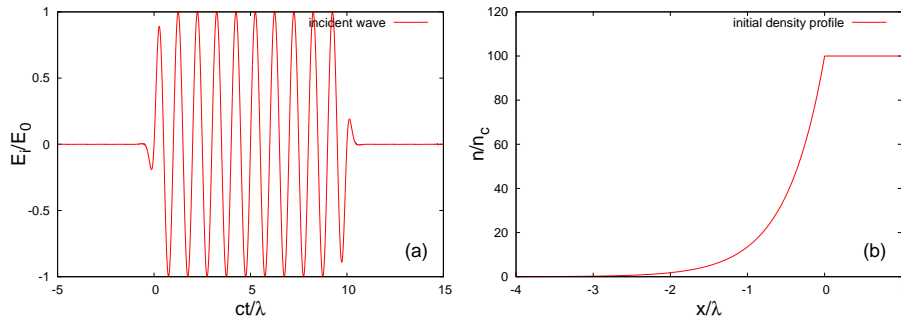


Figure 1: (a) Electric field component of the incident electromagnetic wave in vacuum plotted versus time at  $x = 0$ . (b) Initial density profile  $\sigma = 0.5\lambda$ ,  $n_0 = 100n_c$ , where  $n_c$  is the critical density.

plasma density ramp for  $x < 0$ . For  $x > 0$  the density remains constant (Fig.

1b),

$$n(x) = \begin{cases} n_0 e^{\frac{x}{\sigma}} & \text{for } x < 0 \\ n_0 & \text{for } x > 0 \end{cases}. \quad (1)$$

Assuming that the ions are at rest during the whole interaction process, we consider only the interaction between the electrons and the incident wave. In the simple case of normal incidence there are two forces acting on particles along  $x$ -axis. The electrostatic force proportional to  $E_x$  and laser ponderomotive force oscillating with  $2\omega$  (twice of the laser frequency). Thus the plasma surface oscillates with the half of the laser period (Fig. 2 (a)). In the case of oblique

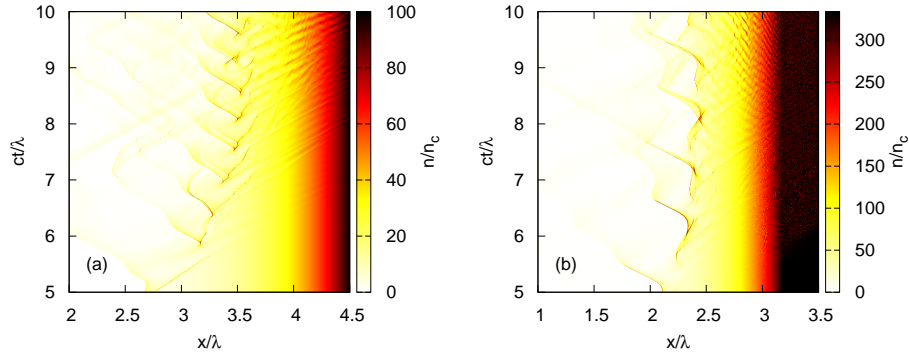


Figure 2: The electron density distribution in space time domain by (a) normal incidence and (b)  $48^\circ$  oblique incidence. Simulation parameters considering from the laboratory frame are: plasma density  $n_0 = 100n_e$ ,  $\sigma = 0.5\lambda$ ; laser amplitude  $a_0 = 10$ . Note that the values in (b) are transformed concerning to the moving frame.

incidence of a p-polarized wave, there is going to be an additional longitudinal component of the electric field oscillating at frequency  $\omega$  and acting on the plasma surface. Consequently the interaction becomes even more complicated, which leads to stronger oscillations of the plasma surface containing both  $\omega$  and  $2\omega$  modes (Fig. 2 (b)).

As soon as the electrons are pulled back by the electrostatic force, they form a thin nanobunch that reaches a velocity close to  $c$ . In this case the generation of high harmonics is possible.

### 3 Density profile of a thin electron layer

In this section we do the first step towards our first goal described in the introduction and derive two different analytic expressions for two different cases, which roughly describe the electron density profile at the times where the sharp spikes appear. The starting point of our calculations is the approximation of the electron phase space distribution at these times. As we shall see later this

distribution depends on the propagation velocity  $\dot{x}_0(t)$  of the given electron layer.

First, let us consider the case of a slow electron bunch  $\dot{x}_0(t) \ll c$ . In

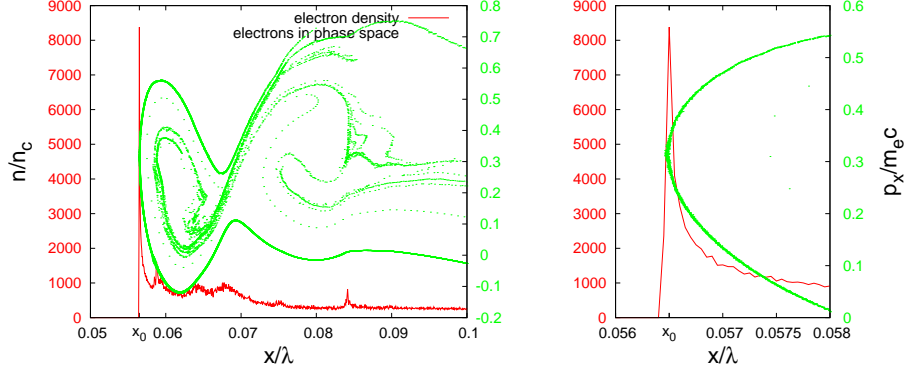


Figure 3: Electron density (red) and electrons in  $x$ - $p_x$ -plane (green).  $x_0$  is the position of the maximal density. Simulation parameters: initial plasma density  $n_0 = 241n_c$ ;  $\sigma = 0.001\lambda$ , Pulse with dimensionless amplitude  $a_0 = 10$  and p-polarized oblique incidence at  $57^\circ$  angle has the wave length  $\lambda = 820\text{nm}$ . All magnitudes are taken in the simulation frame. The right picture gives a zoom of the area around  $x_0$ .

Fig. 3 the electron density and its distribution in  $x$ - $p_x$ -phase space at time  $t = 0.875\lambda/c$ , when the electrons are pushed inside the plasma almost to the maximal distance by the ponderomotive force are visualized. We count the time according to Fig. 1 (Fig. 1a shows the field oscillations at the point  $x = 0$  where the region with the constant plasma density begins (Fig. 1b)). Because we start with a cold plasma, the electron distribution function is a (curved) line in the phase space. We assume that this curve in phase space is described by the function  $x(p)$  at some small interval close to the density spike. Obviously,  $x_0$  is the local minimum of this function that coincides with the position of the spike. In fact, we have always a spike of electron density at the point, where the function  $x(p)$  exhibits the local extreme value. For instance, if we take a look at another curve in phase space, which is enclosed by the previous one, we see that there is also a local maximum of the density at the point where the curve reaches its minimal  $x$ -value. However the electrons are more scattered (heated) compared to the previous case and thus the local density maximum is much smaller. The idea, that gives us the starting point for our calculations is the following one. We can locally describe given curve in phase space as a parabola:

$$x(p, t) = x_0(t) + \alpha(t)(p - p_0(t))^2. \quad (2)$$

The point  $(x_0(t), p_0(t))$  corresponds to the local minimum. We consider some short interval  $\Delta x$  where this assumption makes sense. Starting from this assumption and doing some algebra we obtain the expression for electron density profile

$$n(x, t) = \frac{1}{2} \frac{N}{\sqrt{\Delta x (x - x_0(t))}}, \quad (3)$$

where  $N$  is the number of particles contained between  $x_0(t)$  and  $x_0(t) + \Delta x$ . Note that the parameter  $\alpha$  cancels out, so it does not affect the density profile.

The derivation of this expression is shifted to the appendix A. In Fig. 4 we

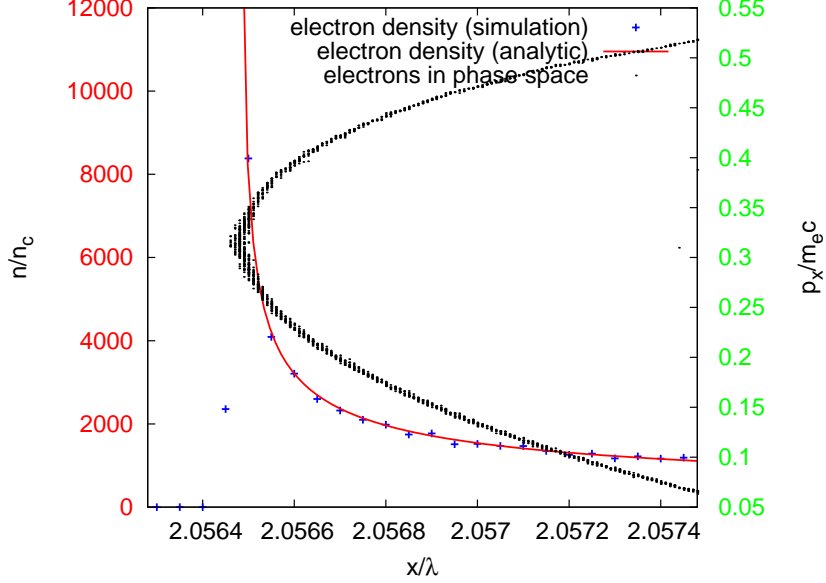


Figure 4: Electron density taken from simulation (blue) and calculated analytically via (3) (red), as well as electrons in  $x$ - $p_x$ -plane (black), with same simulation parameters as for Fig. 3,  $\Delta x = 0.001\lambda$  (simulation frame).

see that the density described with (3) agrees very well with simulation results. This picture is actually a zoom of the Fig. 3 at the position of density spike. We obtain the best agreement at the instants when the electrons are pushed inside at the maximal distance. In this case, the mean momentum of the electrons is close to zero and equation (2) describes electrons in phase space quite well. We call the case where  $\dot{x}_0(t) \ll c$  is valid “parabolic case”.

Now we discuss another case with  $\dot{x}_0(t) \rightarrow c$ . Consider the phase space evolution taken from the other simulation illustrated in Fig. 5. At the beginning,  $t = 6.2\lambda/c$ , the momentum is close to zero and the distribution is parabolic as expected. Further, as soon as the electron bunch is pulled back by the electrostatic force, the negative momentum of the bunch grows constantly with time and the distribution changes its form until it becomes a kind of a “whip” between  $t = 6.5\lambda/c$  and  $t = 6.6\lambda/c$ . The extremely dense electron nanobunch reaches the velocity close to  $c$  during this period. This picture is taken from the same simulation as Fig. 2 (b). In this case the phase space distribution can be roughly fitted with an exponential function

$$x_p(p, t) = x_0(t) + e^{\alpha(t)(p-p_0(t))} \quad (4)$$

(see Fig. 6). As we will show later, the incident angle and the density gradient that were used here are optimal for producing the most intense attosecond pulse. The phase space distribution belongs to the nanobunch that emits this pulse. In order to simplify the notation we drop the time dependence and set  $p_0 = x_0 = 0$ . At this point we have

$$x_p(p) = e^{\alpha p}. \quad (5)$$

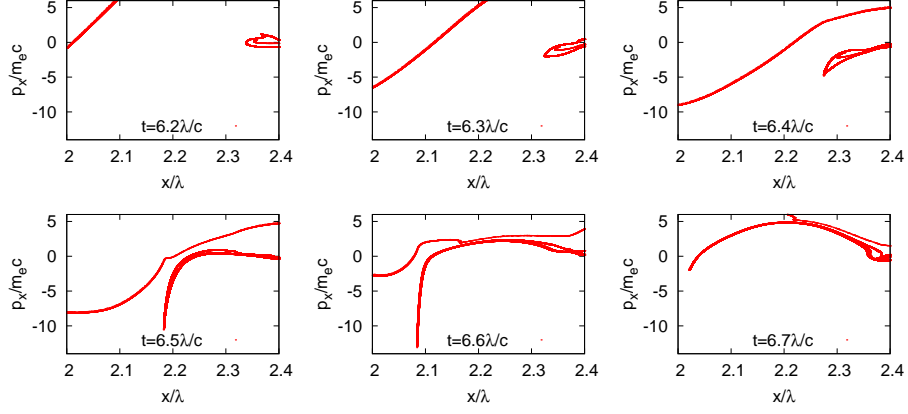


Figure 5: Electrons in  $x$ - $p_x$ -plane taken from the simulation to different times  $t$  during the process of nanobunching. Simulation parameters: initial plasma density  $n_0 = 100n_c$ ;  $\sigma = 0.5\lambda$  (laboratory frame), Pulse with dimensionless amplitude  $a_0 = 10$  and p-polarized oblique incidence at  $48^\circ$  angle has the wave length  $\lambda = 820\text{nm}$ .

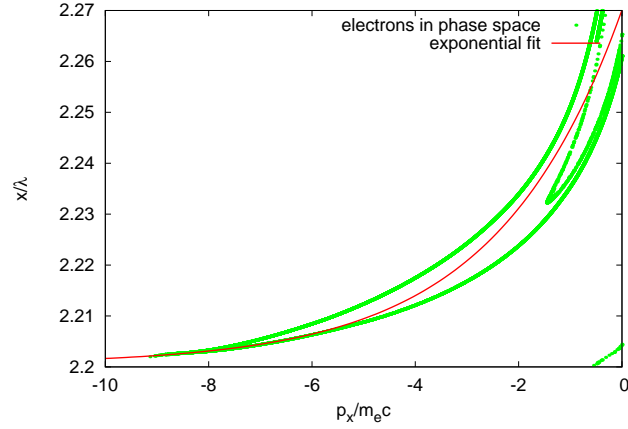


Figure 6: Electrons in  $x$ - $p_x$ -plane (green) and the exponential fit (red) from the same simulation as Fig. 5, taken to the time  $t = 6.48\lambda/c$ .

On some short interval  $[x_{\min} : x_{\max}]$  the density profile can be calculated to

$$n(x) = \frac{N}{\ln\left(\frac{x_{\max}}{x_{\min}}\right)x}, \quad (6)$$

where  $N$  is the number of particles contained between  $x_{\min}$  and  $x_{\max}$ . A technical details are shifted to the appendix A. As we can see from Fig. 7 equation (6) approximates the density profile quite well even over the comparably long interval. We call the case where  $\dot{x}_0(t) \rightarrow c$  is valid “whip case”.

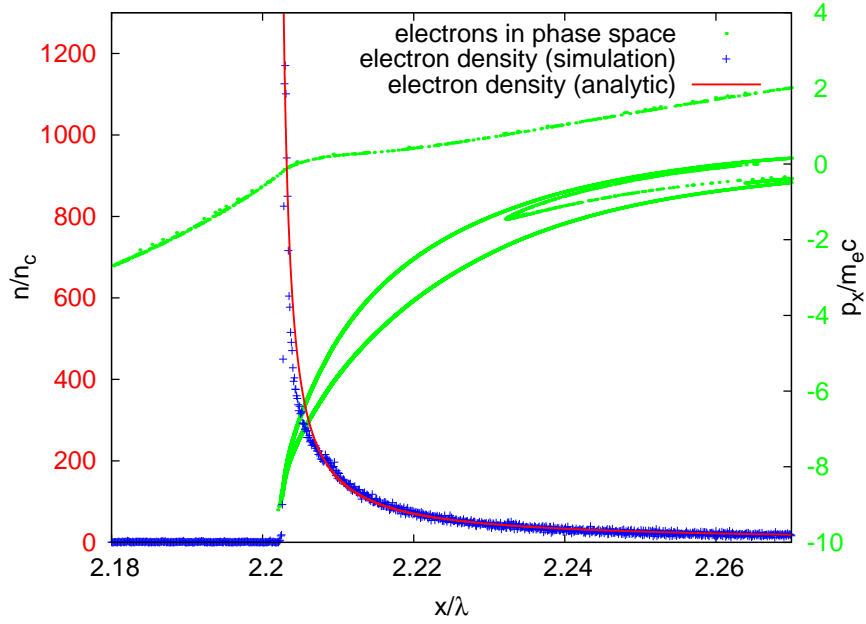


Figure 7: Electron density taken from simulation (blue) and calculated analytically via (6) (red), as well as electrons in  $x$ - $p_x$ -plane (green), with same simulation parameters compared to Fig. 5, taken at  $t = 6.48\lambda/c$ .  $x_{\min} - x_0 = 8,5 \cdot 10^{-4}\lambda$ ;  $x_{\max} - x_0 = 0.05\lambda$  (simulation frame).

Although the functions (3) and (6) work well on the given intervals, we still have the problem that they both are not continuous or even exhibit a singularity. Such behavior is obviously not physical. In fact we are able to describe only a part of the spike correctly. In order to solve this problem we need to find an expression that would describe the whole spike. That means for instance on interval  $[x_0 - \Delta x : x_0 + \Delta x]$ . In order to find such function we have to replace the delta function, which is used for the definition of the distribution function in equations (28) and (34) by some limited function  $\delta_a(x)$  with

$$\lim_{a \rightarrow 0} \delta_a(x) = \delta(x). \quad (7)$$

The parameter  $a$  describes the width of  $\delta_a$ , which means that  $a > 0$  is required. One of the possible definitions of  $\delta_a$  leads to the solution



$$n_{a,\Delta x}(x) = \begin{cases} \frac{N_{a,\Delta x}}{5a^3\sqrt{\Delta x}} (3a^2 - 2x^2 + ax) \sqrt{x+a} & \text{for } x \in [-a, a] \\ \frac{N_{a,\Delta x}}{5a^3\sqrt{\Delta x}} \left( (3a^2 - 2x^2) (\sqrt{x+a} - \sqrt{x-a}) + ax (\sqrt{x+a} + \sqrt{x-a}) \right) & \text{for } x > a \\ 0 & \text{for } x < -a \end{cases} \quad (8)$$

See appendix A for more details.

Now let us try to fit the simulated density from above with the calculated analytical profile (Fig. 8). We chose a quite small value for  $a$  because the plasma

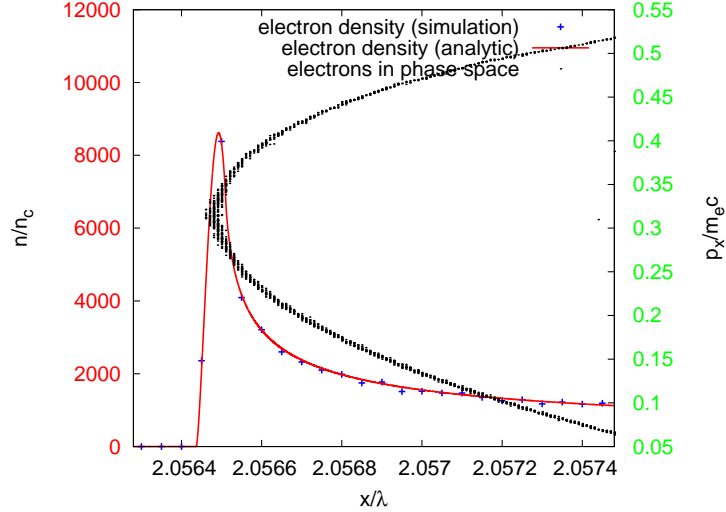


Figure 8: Electron density taken from the simulation (blue) and calculated analytically via (8) (red), with same simulation parameters as for Fig. 3,  $\Delta x = 0.001\lambda$ ;  $a = 3,7 \cdot 10^{-5}$  (simulation frame).

is cold and we are dealing with very big and sharp spike as it is shown in this example. This is the case since we use strong laser pulse and very small cell size ( $5 \cdot 10^{-5}\lambda$ ). As we can see, our function agrees well with the simulated profile.

Of course the generalization  $\delta(x) \rightarrow \delta_a(x)$  can be also used to calculate the density in the whip case where  $x_p(p) = e^{\alpha p}$ . But now we have to take  $p_{\text{cut}}$  as a lower limit by the integration (35), since otherwise the integral would diverge for  $x \in [x_{\text{min}} - a, x_{\text{min}} + a]$ . Doing the same steps as in the previous case, we

finally obtain the density profile

$$n_a(x) = \begin{cases} \frac{3N}{4a^3 \ln\left(\frac{x_{\max}}{x_{\min}}\right)} \left( (x+a) \left( x + (x-a) \left( \frac{1}{2} + \ln\left(\frac{x_{\min}}{x+a}\right) \right) \right) \right. \\ \quad \left. + x_{\min} \left( \frac{1}{2}x_{\min} - 2x \right) \right) & \text{for } x \in [x_{\min} - a, x_{\min} + a] \\ \frac{3N}{4a^3 \ln\left(\frac{x_{\max}}{x_{\min}}\right)} \left( 2ax - (x^2 - a^2) \ln\left(\frac{x+a}{x-a}\right) \right) & \text{for } x > x_{\min} + a \\ 0 & \text{for } x < x_{\min} - a \end{cases} \quad (9)$$

Now as in the previous case we are going to compare the calculated analytical function with the simulated density profile (Fig. 9). Again we obtain good

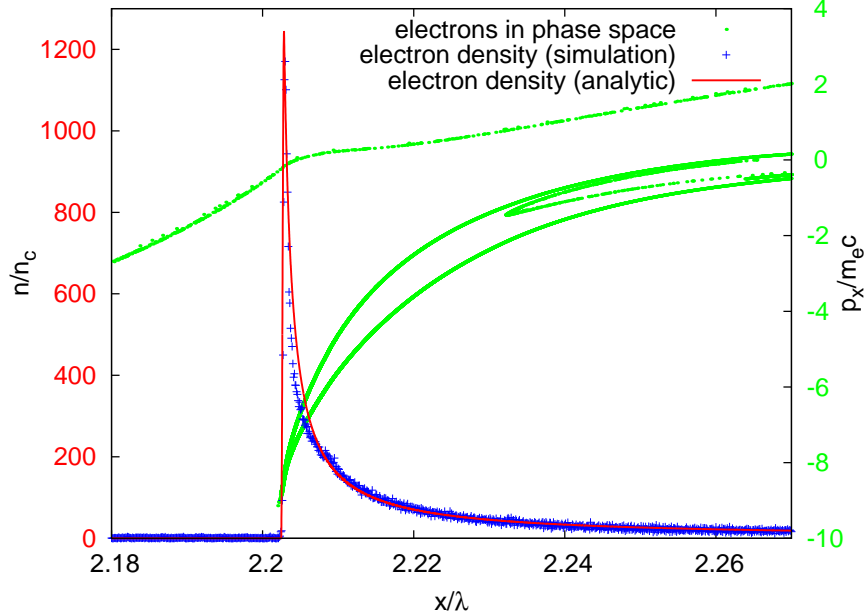


Figure 9: Electron density taken from simulation (blue) and calculated analytically via (9) (red), as well as electrons in  $x$ - $p_x$ -plane (green), with same simulation parameters compared to Fig. 5, taken at  $t = 6.48\lambda/c$ .  $x_{\min} - x_0 = 8,5 \cdot 10^{-4}\lambda$ ;  $x_{\max} - x_0 = 0.05\lambda$ ;  $a = 2 \cdot 10^{-4}$  (simulation frame).

agreement and are able to describe the density spike quite well.

Before we go further, we analyze the intermediate case  $\dot{x}_0(t) \lesssim c$ . In this case, the electron phase space distribution looks like it is shown in Fig. 10 and can not be approximated well neither with a parabolic, nor with an exponential function. Nevertheless, we find out that the density profile of the spike can still be well approximated with equation (8) (Fig. 10), so we classify the cases with intermediate velocities as parabolic. Fig. 10 is taken from the same simulation as Fig. 8, but at the later time.

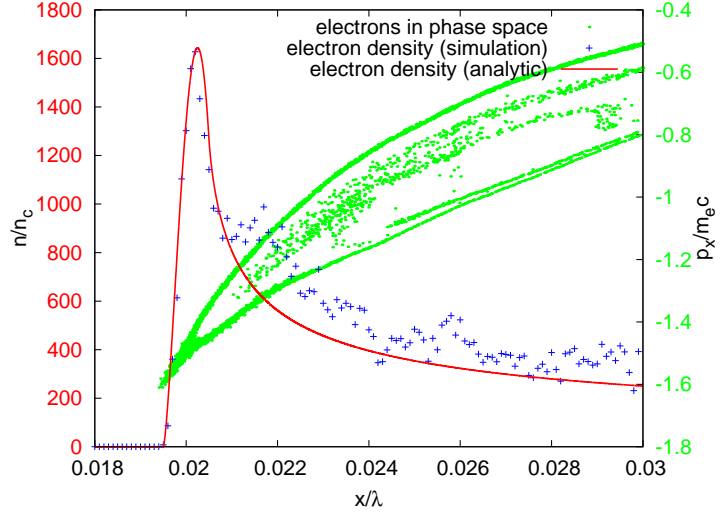


Figure 10: Electron density taken from simulation (blue) and calculated analytically via (8) (red), as well as electrons in  $x$ - $p_x$ -plane (green), with same simulation parameters compared to Fig. 3 but to the later time with parameters  $\Delta x = 0.01\lambda$ ;  $a = 5 \cdot 10^{-4}$  (simulation frame).

In the following chapter we are going to analyze the corresponding simulation results more extensively. We will use the descriptions of the electron layer density profile derived here in order to calculate an expression for the spectra of the reflected waves in different cases.

## 4 Electron density evolution and HHG emission

In the previous section, we did the first step towards our aim to improve the analytical description of the spectrum in the case of CSE. We derived two analytic expressions which describe the electron density profile in two different cases during CSE process. In this section we will go further and work out the equations for the transverse current distribution for the corresponding cases, where the expressions derived previously will be used. Since the reflected radiation  $E_r(t)$  is determined by the transverse current distribution  $j_\perp(t, x)$  via

$$E_r(t) = \pi \int j_\perp(t - x, x) dx, \quad (10)$$

where we use the normalized PIC units, see [48] for more detail, the results will lead us directly to the improved description of the spectrum (see below). In order to start the derivation, we have to make some assumptions about the current distribution in particular case. For that reason we briefly consider the process of CSE.

We are interested in the high frequency spectrum of the reflected pulse mostly determined by the behavior of the electron nanobunch when it moves away from the plasma with maximal velocity. This moment corresponds to the stationary phase point (SPP) (see [37]). The gamma factor of the bunch exhibits a sharp spike at this time, the so called  $\gamma$ -spike [32]. One distinguishes different orders of  $\gamma$ -spikes depending on behavior of the transverse current (see below).

First, we investigate the example of the whip case ( $\dot{x}_0(t) \rightarrow c$ ) from the previous section illustrated in Fig. 2(b), Fig. 5 and Fig. 9 more extensively. The reflected wave obtained in this simulation is shown in Fig. 11 (a). Since we use a few cycle laser pulse, we get an attosecond pulse train as reflected radiation. In the following, we consider only the most intense reflected pulse  $E_r^{\text{pls}}(t)$  that is filtered out by the Gaussian function (Fig. 11 (b)), i.e.

$$E_r^{\text{pls}}(t) = E_r(t) e^{(t-t_{\text{max}})^2/\tilde{\sigma}^2}, \quad (11)$$

where  $t_{\text{max}}$  corresponds to the maximal wave amplitude and  $\tilde{\sigma} = 0.2\lambda/c$ . The amplitude of the pulse is about five times larger than of incident wave like in the CSE case. The electron nanobunch which radiates this pulse can be clearly recognized from the density distribution shown in Fig. 12. For convenience, we chose the coordinates in Fig. 12 (b) in such a way that the SPP is in the point (0,0), while in Fig. 12 (a) it corresponds to the point  $(2.16\lambda, 6.52\lambda/c)$ .

Now we are able to make some assumption of current behavior in the vicinity of the SPP. Our derivation is similar to the one in [37], but is more detailed. First of all, we assume that the transverse current density does not change its shape during the time and write

$$j_\perp(t, x) = n(t, x)v_\perp(t, x) \approx j(t)f(x - x_0(t)), \quad (12)$$

with density  $n(t, x)$ , velocity  $v_\perp(t, x)$  and the position of the bunch  $x_0$ . The function  $f$  is the shape that is assumed to be constant close to the SPP. If we compare the both sides of the last equation in (12), we can approximate

$$v_\perp(t, x) \approx \bar{v}_\perp(t), \quad n(t, x) \approx n_m f(x - x_0(t)). \quad (13)$$

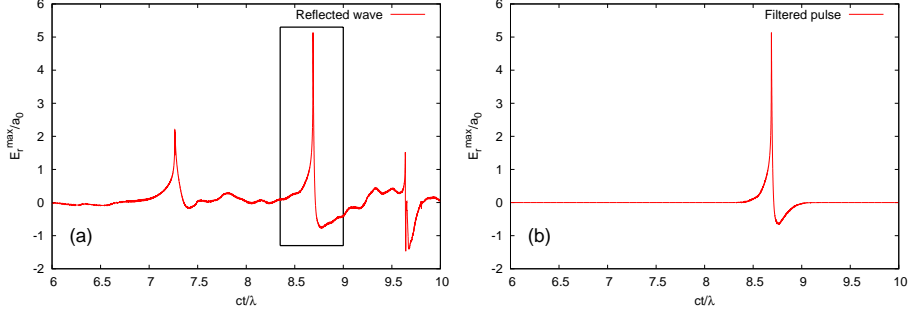


Figure 11: (a): Part of the reflected radiation given by  $\frac{1}{2}(E_y(t) - B_z(t))$ . (b): Single pulse from the reflected pulse train filtered out by the Gaussian function. Simulation parameters are the same as for Fig. 5.

This means that equation (12) assumes the transverse velocity being approximately constant in space and equal to the mean velocity  $\bar{v}_\perp(t)$ . The density profile has a constant shape with the maximal value  $n_m$  and only changes its position  $x_0(t)$ . Thus the equation (12) takes the form

$$j_\perp(t, x) \approx n_m \bar{v}_\perp(t) f(x - x_0(t)), \quad j(t) = n_m \bar{v}_\perp(t). \quad (14)$$

In the next step, we assume the ultrarelativistic regime, which means that absolute velocity of the particles is always close to  $c$ . In this case we can write

$$\sqrt{\dot{x}_0(t)^2 + \bar{v}_\perp(t)^2} \approx v \approx c \quad (15)$$

Now we are going to Taylor expand  $j(t)$ . Let us first take a look at the Fig. 13 (a). It shows the transverse current distribution of the given nanobunch. In the SPP the bunch exhibits maximal longitudinal velocity  $v_x = v$  which is close to  $c$ , so that the transverse component almost vanish. As a result, the transverse current vanishes as well. This can be seen in the picture. We can also see, that the current does not change its sign at the SPP. So we assume

$$j(t) \approx \alpha_0 t^2. \quad (16)$$

Combining this relation with the second equation from (14) and inserting it in (15) leads to

$$\begin{aligned} \dot{x}_0(t) &\approx -\sqrt{v^2 - \frac{\alpha_0^2}{n_m^2} t^4} \approx -v + \frac{\alpha_0^2}{2vn_m^2} t^4, \\ x_0(t) &\approx -vt + \frac{\alpha_0^2}{2vn_m^2} \frac{t^5}{5} \equiv -vt + \alpha_1 \frac{t^5}{5}. \end{aligned} \quad (17)$$

Here we have the negative sign in front of the square root since the electron layer moves in the negative direction. To describe the shape  $f$  we use the expression for the density profile (9) which is derived in the previous section. With this function we replace the Gaussian function that is used in [37]. Obviously the function (9) fits the density much better than the Gaussian function as shown above. From the second equation of (13), we read that the maximal value of  $f$

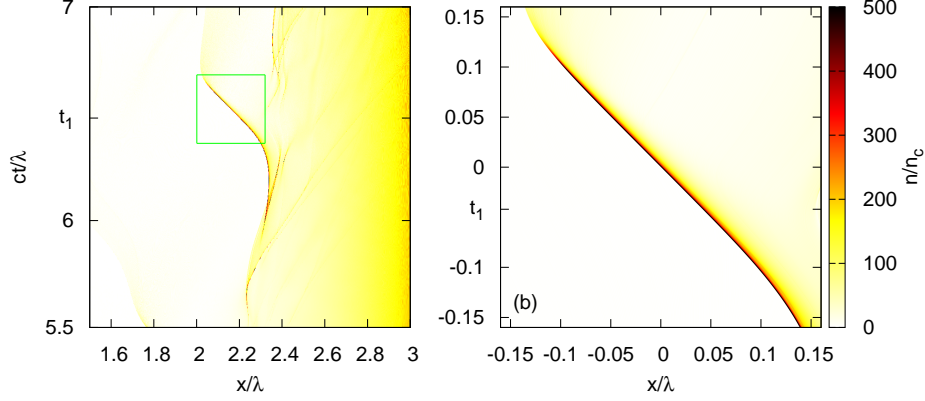


Figure 12: The electron density distribution in space time domain. Simulation parameters are the same as for Fig. 5. All magnitudes are taken in the simulation frame. The green square in (a) marks the nanobunch that is zoomed in (b). This bunch is responsible for the radiation of the strong pulse shown in Fig. 11. In (a)  $t_1 = 6.48\lambda/c$  as in Fig. 9.

is one. Consequently we conclude, that

$$f(x) = \frac{1}{n_m} n_a(x).$$

Since  $n_m$  should represent the maximum of  $n_a$ , we can write  $n_m = n_a(x_m)$ , where  $x_m$  is the extrem value of  $n_a$ , which depends on parameters  $a$  and  $x_{\min}$ . In addition we multiply the shape function with a wider Gaussian function since  $f$  decays too slowly ( $\propto 1/x$ ) for positive  $x$  and after certain  $x$ -value does not coincide with the given density. Thus the Gaussian helps as to cut this “tail” with no influence on the spectrum structure. So we have

$$f(x) = \frac{n_a(x)}{n_a(x_m)} e^{-\frac{x^2}{\sigma^2}}. \quad (18)$$

Now, we just need to insert the equations (16), (17) and (18) in (12) in order to obtain the analytical expression of the current distribution. To get some result we need to choose the parameters contained in this formulas, in the way that the calculated distribution would be similar to those we obtained from simulation (Fig. 13 (a)). Moreover, the physical values like the maximal density  $n_m$  or maximal velocity  $v$  have to be in line with the simulation results. We find that the parameter set we used to obtain Fig. 13 (b) is a good choice.

First of all, we see that the analytical current distribution fits the original one quite well (Fig. 13). From the bottom pictures in Fig. 13 we see that the width and the trajectory of the current peak are well predicted by the analytical model. The corresponding maximums can considerably deviate at some points like at  $t = -0.05\lambda/c$  and  $t = 0.1\lambda/c$  but still remain at the same order of magnitude. The current also does not vanish completely at the SPP as expected for the ideal

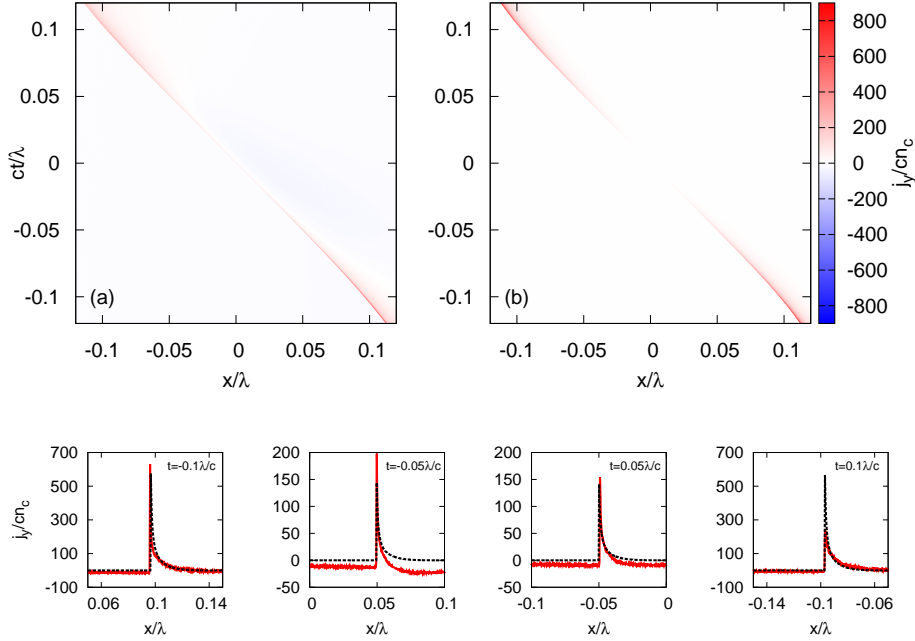


Figure 13: Transverse current density from the simulation (a) and calculated analytically (b). In (a) the simulated current density near the SPP (0,0) is illustrated. As we see the transverse current almost vanish in SPP. Simulation parameters are the same compared to Fig. 5. In (b) the analytically calculated current distribution is shown. The parameters used in equation (17) are:  $\alpha_0 = 6 \cdot 10^4$ ,  $n_m = 1100$  and  $\gamma = 15$ , while the parameters used for the shape are:  $a = 1, 5 \cdot 10^{-4} \lambda$ ,  $x_{\min} = 8 \cdot 10^{-4} \lambda$  and  $\tilde{\sigma} = 0.02 \lambda$ . The velocity  $v$  in (17) is derived from the given gamma factor. Bottom pictures illustrate the simulated (red) and calculated (black) current at the reference times  $-0.1\lambda/c$ ,  $-0.05\lambda/c$ ,  $0.05\lambda/c$  and  $0.1\lambda/c$ .

case, but reaches the minimum of about  $60cn_c$ . The chosen maximal density  $n_m$  is in line with simulation as can be seen from Fig. 9. In order to have an idea concerning the order of magnitude of gamma factor, we visualized the distribution of  $\gamma$  in the vicinity of density spike (Fig. 14). As we see  $\gamma$  almost reaches the value  $\gamma = 15$ . The numbers  $a$  and  $x_{\min}$  that characterize the shape are similar to those we used in Fig. 9. They are slightly different because these numbers pass better for fitting the current density through some finite time interval, while in case of Fig. 9 only one particular time point is considered.

Now we consider the radiation emission from the assumed current distribution as well as its spectrum. Equation (10) enables us to calculate the radiation and the spectrum analytically. Here we give the expression of radiated spectrum

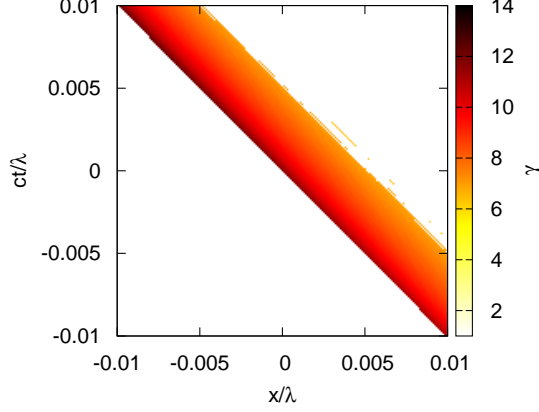


Figure 14: Distribution of  $\gamma$  factor in the given nanobunch calculated only in cells with density bigger than  $200n_c$ .

that is derived in line with [37].

$$I(\omega) = E_r^2(\omega) = 4\pi^4 \alpha_0^2 (\alpha_1 \omega)^{-\frac{6}{5}} \left( Ai_2''(\alpha_1^{-\frac{1}{5}} \delta \omega^{\frac{4}{5}}) \right)^2 |f(\omega)|^2, \quad (19)$$

$$\alpha_1 = \frac{a_0^2}{2vn^2}, \quad \delta = 1 - v, \quad Ai_2'' = \frac{d^2}{dx^2} \frac{1}{2\pi} \int e^{i\left(xt + \frac{t^5}{5}\right)} dt.$$

The Fourier transform of the shape function  $f(\omega)$  is calculated numerically using FFT. In Fig. 15 (b) the spectrum calculated using (19) is compared with the spectrum calculated from original reflected pulse (Fig. 11) via FFT. Obviously the description works very well almost until 1000-th harmonic. The both graphs diverge for  $\omega < 100\omega_0$  but anyway the method of SPP used here works only for high harmonics, so we may not expect the coincidence for low frequencies. In

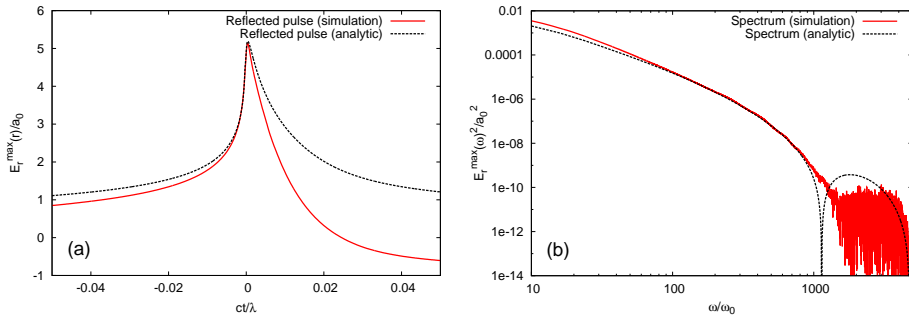


Figure 15: Reflected radiation obtained from the simulation ((a) red) and from analytical current distribution ((a) black), as well as the corresponding spectra in (b). The spectrum from the simulation is taken directly from the radiated pulse via FFT, while the other one is obtained using the equation (19).



Fig. 15 (a) the corresponding pulses are compared. So the red one is the same as shown in Fig. 11 and the black one is determined from the assumed analytical current distribution using (10). The bough graphs behave in the similar manner. To conclude, we can say that we obtained quite good results applying our new shape function derived in the previous section instead of a Gaussian function.

Going along the same line we analyze now the intermediate case  $\dot{x}_0(t) \lesssim c$  shown in Fig. 10. As said before, we attribute this case to the parabolic case. First of all, we consider the reflected pulse train and filter out the pulse we are interested in (Fig. 16). The density and the gamma factor of the corresponding

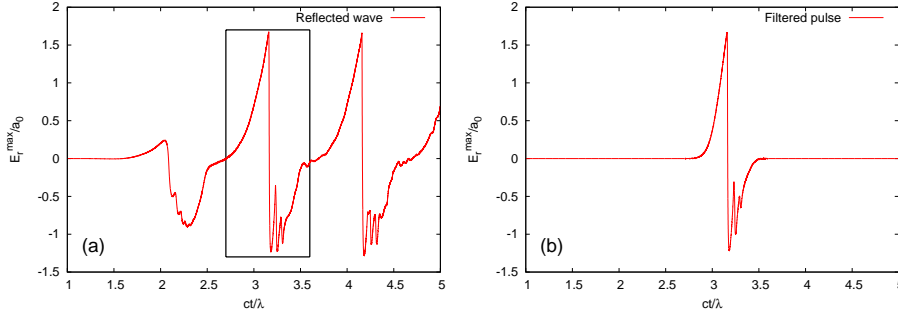


Figure 16: (a) Part of the reflected radiation given by  $\frac{1}{2}(E_y(t) - B_z(t))$ . (b) Single pulse from the reflected pulse train filtered out by the Gaussian function. Simulation parameters are the same as for Fig. 3.

electron bunch is shown in Fig. 17. The point (0,0) corresponds to the SPP like

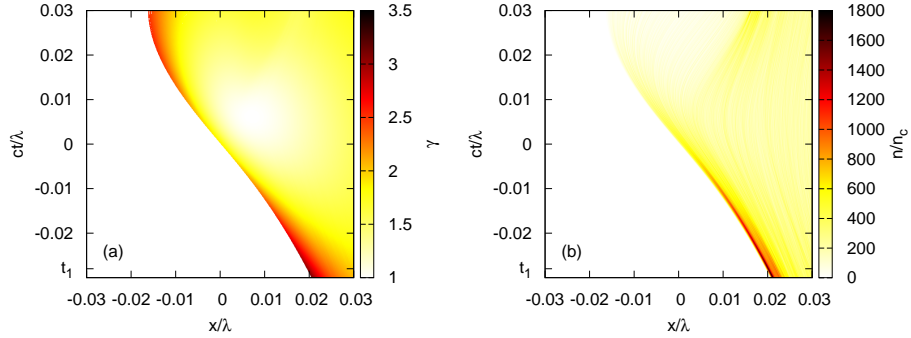


Figure 17: (a) Distribution of the gamma factor in the given electron bunch in space time domain. (b) The electron density distribution in space time domain. Simulation parameters are the same compared to Fig. 3. All magnitudes are taken in the simulation frame.  $t_1$  denotes the time which corresponds to Fig. 10,  $t_1 = -0.028\lambda/c$ .

in the previous case. Even from this picture one can clearly see that the velocity in the SPP significantly deviates from the speed of light and is approximately  $0.85c$ . From the distribution of the gamma factor we see that it is roughly constant within the electron layer. So we can use the same approximation as in

the previous case

$$\sqrt{\dot{x}_0(t)^2 + \bar{v}_\perp(t)^2} \approx v. \quad (20)$$

The difference between (15) and (20) is of course that in the last equation  $v$  is not close to  $c$ . For that reason the electron phase space distribution does not become “whip-like” (Fig. 10).

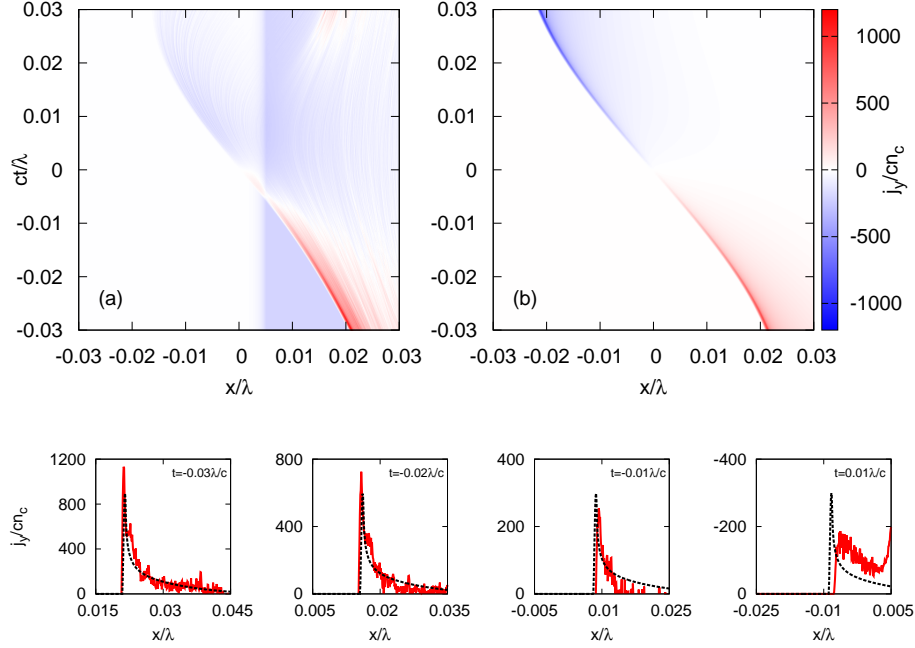


Figure 18: Transverse current density from the simulation (a) and calculated analytically (b). In (a) the simulated current density near the SPP is illustrated. Simulation parameters are the same compared to Fig. 3. In (b) the analytically calculated current distribution is shown. The parameters used in equation (22) are:  $\alpha_0 = 3 \cdot 10^4$ ,  $n_m = 1000$  and  $\gamma = 2$ , while the parameters used for the shape are:  $a = 4 \cdot 10^{-4} \lambda$  and  $\tilde{\sigma} = 0.02 \lambda$ . The velocity  $v$  in (17) is derived from the given gamma factor. Bottom pictures illustrate the simulated (red) and calculated (black) current at the reference times  $-0.03 \lambda/c$ ,  $-0.02 \lambda/c$ ,  $-0.01 \lambda/c$  and  $0.01 \lambda/c$ .

Now let us consider the corresponding current distribution (Fig. 18(a)). In this case, the current changes its sign in the SPP, so we can assume

$$j(t) \approx -\alpha_0 t. \quad (21)$$

Similar to the previous case, we derive

$$x_0(t) \approx -vt + \frac{\alpha_0^2}{2vn_m^2} \frac{t^3}{3} \equiv -vt + \alpha_1 \frac{t^3}{3}. \quad (22)$$

Using these assumptions we calculate the current distribution analytically (Fig. 18(b)). In this case we obtain a good agreement only for negative times (see

bottom pictures of Fig. 18), but the predicted trajectory of the peak is still close to original one. The gamma factor can be roughly read from Fig. 17, so we set  $\gamma = 2$ . This value matches well the maximum longitudinal velocity of the layer obtained above. Finally we obtain the spectrum of the reflected wave

$$I(\omega) = E_r^2(\omega) = 4\pi^4 \alpha_0^2 (\alpha_1 \omega)^{-\frac{4}{3}} \left( Ai_1'(\alpha_1^{-\frac{1}{3}} \delta \omega^{\frac{2}{3}}) \right)^2 |f(\omega)|^2, \quad (23)$$

$$\alpha_1 = \frac{a_0^2}{2vn^2}, \quad \delta = 1 - v, \quad Ai_1' = \frac{d}{dx} \frac{1}{2\pi} \int e^{i\left(xt + \frac{t^3}{3}\right)} dt.$$

The corresponding pulses and their spectra are shown in Fig. 19. Even if the

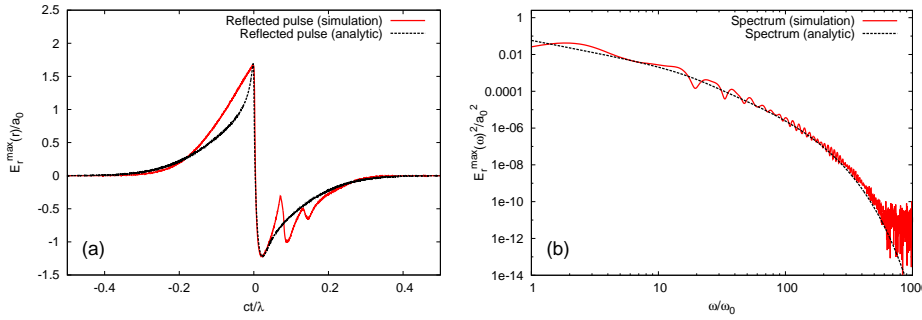


Figure 19: Reflected radiation obtained from the simulation ((a) red) and from analytical current distribution ((a) black), as well as the corresponding spectra in (b). The spectrum from the simulation is taken directly from the radiated pulse via FFT, while the other one is obtained using the equation (23).

above assumptions did not work as good as in the previous case, the obtained results still give a satisfactory approximation.

We can generalize the equations (19) and (23) and write:

$$I(\omega) = E_r^2(\omega) = 4\pi^4 \alpha_0^2 (\alpha_1 \omega)^{-\frac{2n+2}{2n+1}} \left( \frac{d^n}{d\xi^n} Ai_n(\xi_n) \right)^2 |f(\omega)|^2,$$

$$\xi_n = \alpha_1^{-\frac{1}{2n+1}} \delta \omega^{\frac{2n}{2n+1}}, \quad Ai_n = \frac{1}{2\pi} \int e^{i\left(xt + \frac{t^{2n+1}}{2n+1}\right)} dt.$$

We obtain this formula from the general assumption  $j(t) = \alpha_0(-t)^n$  for the transverse current. The index  $n$  corresponds to the order of a certain  $\gamma$ -spike. Thus, we see that in the first example (whip case) we have the second order gamma spike, while in the second example (parabolic case) the first order gamma spike is obtained.

Now it is time to deal with our second goal, namely to investigate the most efficient case of HHG at moderate laser intensity ( $a_0 = 10$ ). For this purpose we perform several 1D PIC simulations and vary the steepness of the exponential density gradient as well as incident angle. For each parameter set we consider the reflected radiation in order to find the increase of the amplitude that is common in the case of nanobunching. In Fig. 20 we visualized the maximal amplitude of the reflected wave for each parameter set respectively. Consider the incident angle between 45 and 60, since by this angles the most interesting things happen. Of course, one notices the sharp increase of the reflected wave

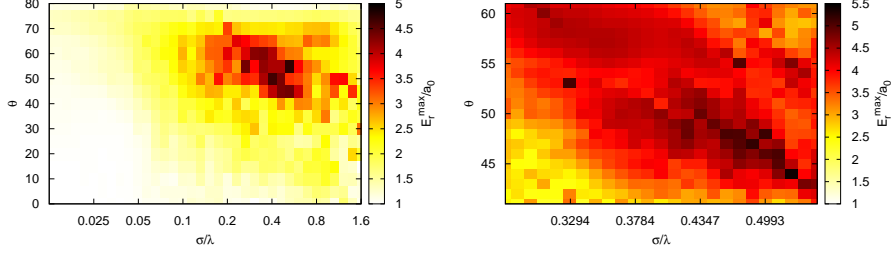


Figure 20: Each point in these pictures corresponds to the maximal amplitude obtained from the reflected radiation taken from corresponding simulation. We have different angles of incidence along  $y$ -axis and different steepness of the density gradient along  $x$ -axis, where  $\sigma$  is taken from (1) and  $n_0 = 100n_c$  (laboratory frame). The right picture is the zoom in the parameter range where the most strong amplification is obtained.

amplitude in the area around  $\sigma = 0.4\lambda$  zoomed in Fig. 20(b). By  $\sigma = 0.5\lambda$  and the angle  $48^\circ$  (laboratory frame) we get the amplification of a factor of five. This is the most efficient HHG we could obtain. We call this area high amplitude parameter set (HAPS). In this area we mostly obtain the second order  $\gamma$ -spikes and the current does not change its sign in the SPPs like in Fig. 13. Furthermore, our study shows that the maximum longitudinal velocity of the boundary electron layer increases monotonically with  $\sigma$  until HAPS, where it almost reaches  $c$ . For  $\sigma < 0.05\lambda$  the boundary oscillates too slowly so that no short pulses are generated. Roughly in the range between  $0.05\lambda$  and  $0.1\lambda$  we obtain the reflected radiation very similar to that from Fig. 16 and generated via the same mechanism. We call this area moderate amplitude parameter set (MAPS). Here we have only first order  $\gamma$ -spikes and the current changes sign in the SPPs. Thus the reflected spectrum in MAPS can be approximated with equation (8) (parabolic case) and the area of HAPS corresponds to the exponential case (equation (9)). In the area between MAPS and HAPS the interaction is too complicated to be attributed to any model.

## 5 Transmitted radiation in nanobunching regime

We considered only reflected radiation until now, but the question if the transmitted radiation could also be described with our model still can be asked. The CSE in transmission has already been obtained by normal incidence on ultra-thin foils [38, 39]. So we performed several simulations using the  $0.2\lambda$  foil and varying the density gradient and the density. By choosing  $\sigma = 0.4$  for the density gradient and a density of  $40n_c$ , we could obtain a transmitted pulse with a maximum amplitude that reaches almost 30% of the incident amplitude (Fig. 21). This pulse is radiated by the electron nanobunch that is accelerated in forward direction and reaches a velocity of  $v \approx 0.95c$  in the SPP (Fig. 22 (b)).

Unfortunately, the electrons are distributed very arbitrarily in phase space in this case (Fig. 23), so there is no chance to apply our analytical formulas for the density spike in this case. The reason of the broad distribution function can be

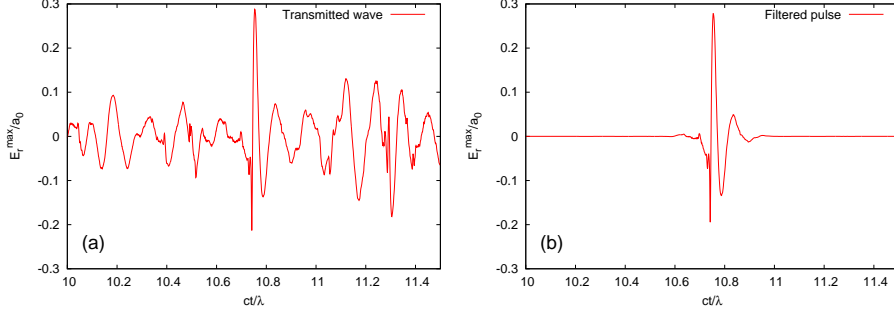


Figure 21: (a) Part of the transmitted radiation. (b) Single pulse filtered out by the Gaussian function. Simulation parameters: initial plasma density  $n_0 = 40n_c$ ;  $\sigma = 0.4\lambda$ , normal incident pulse with dimensionless amplitude  $a_0 = 10$  has the wave length  $\lambda = 820\text{nm}$ .

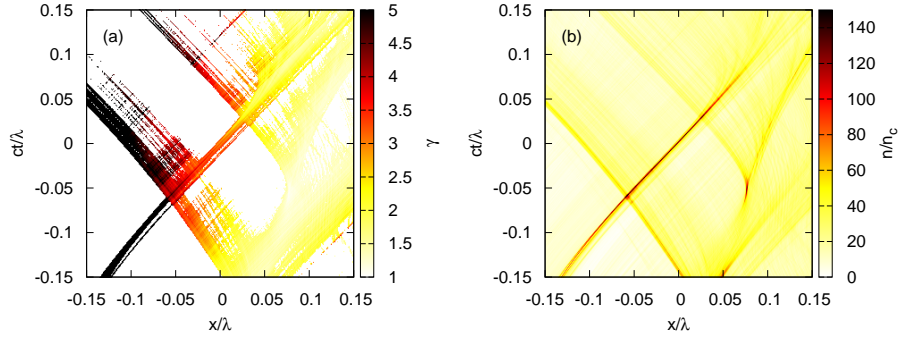


Figure 22: (a) Distribution of the gamma factor in the given electron bunch in space time domain. Gamma factor is shown only for the cells with density above  $20n_c$ . (b) The electron density distribution in space time domain. Simulation parameters are the same as for Fig. 21.

the significant rise of the electron temperature. Instead, the density profile of the considered electron bunch can be roughly described with a simple Gaussian

$$f(x) = e^{-\frac{x^2}{\sigma^2}}. \quad (24)$$

as done in [36, 37]. In Fig. 24 (a) the transverse current distribution of the given electron bunch is demonstrated. We see that the current changes its sign in the SPP, so we use equation (21) here, while  $x_0(t)$  changes its sign compared to (22),

$$x_0(t) \approx vt - \alpha_1 \frac{t^3}{3}. \quad (25)$$

Now we can calculate the current distribution of the bunch that is shown in Fig. 24 (b). In order to calculate the transmitted radiation, we use

$$E_{tr}(t) = \pi \int j_{\perp}(t + x, x) dx, \quad (26)$$

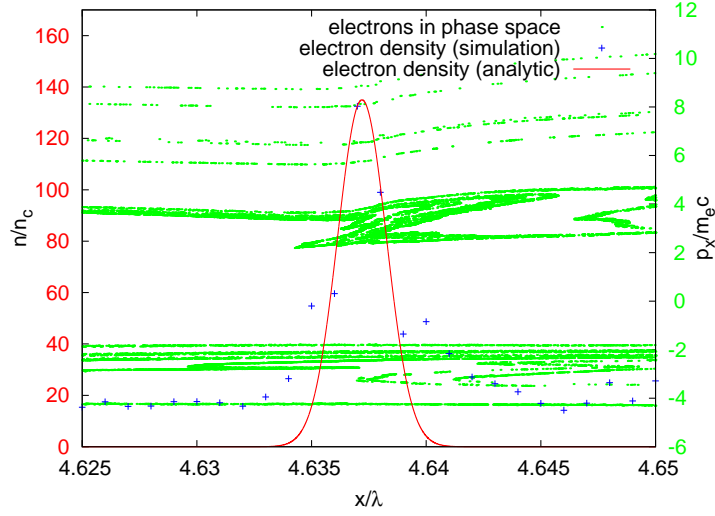


Figure 23: Electron density taken from simulation in SPP (blue) and calculated analytically via (8) (red), as well as electrons in  $x$ - $p_x$ -plane (green), Simulation parameters are the same comparing to Fig. 21, while by analytical description we used  $\tilde{\sigma} = 0.0015\lambda$ .

while the formula for the spectrum is obviously the same as in (23). Since we use a Gaussian function as the shape here, we insert its analytical Fourier image in (23). Subsequently, as in the cases of reflected radiation, we consider the analytical and numerical transmitted pulses as well as their spectra (Fig. 25). It is not very surprising that the results do not fit exactly, especially for the low frequency range. This is because the radiation is formed within the skin layer and has to propagate through whole foil and the trajectory of the radiating electron nanobunch is not anymore in vacuum, but encompasses the bulk plasma.

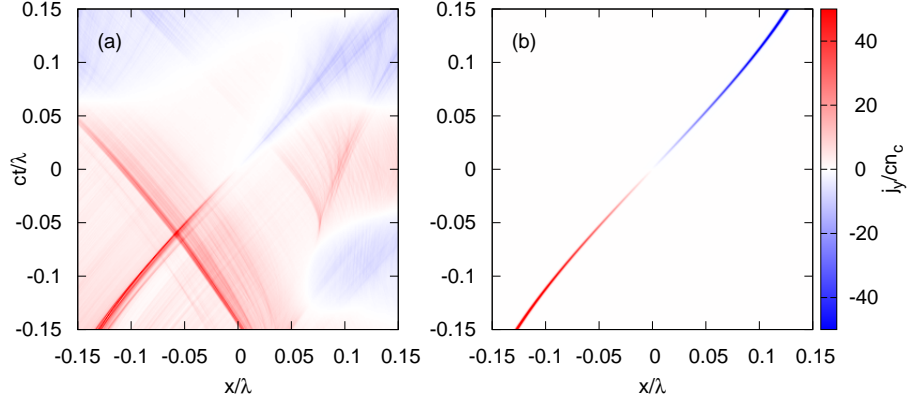


Figure 24: Transverse current density from the simulation (a) and calculated analytically (b). In (a) the simulated current density near the SPP is illustrated. Simulation parameters are the same as for Fig. 21. In (b) the analytically calculated current distribution is shown. The parameters used in equation (22) are:  $\alpha_0 = 500$ ,  $n_m = 100$  and  $\gamma = 3$ , while for the shape we used:  $\tilde{\sigma} = 0.0015\lambda$ . The velocity  $v$  in (17) is obtained from the gamma factor.

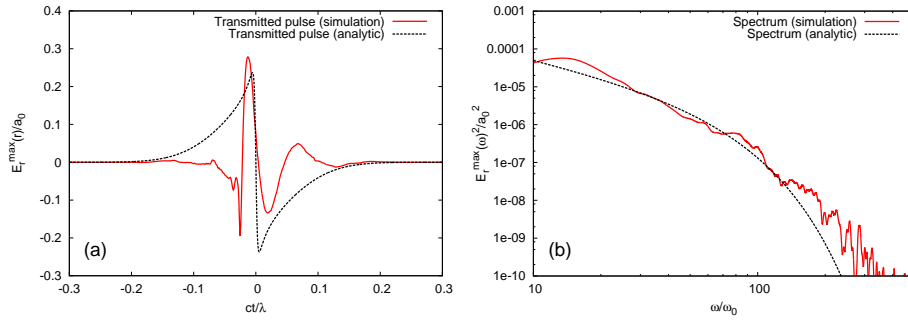


Figure 25: Transmitted radiation obtained from the simulation ((a) red) and from the analytical current distribution ((a) black), as well as the corresponding spectra in (b). The spectrum from the simulation is taken directly from the radiated pulse via FFT, while the other one is obtained using the equation (23).

## 6 Conclusions

We were able to obtain two different analytical expressions of the electron density profile describing the density spikes in two different cases specified by the electron phase space distribution. First, we presented the parabolic case, where the phase space distribution can be approximated by a parabola. In the second case, the electrons in phase space could be fitted with an exponential function. We called this case the whip case. A few examples, where the analytical formulas describe the simulated density quite well have been presented. Furthermore, we discussed simulation results of HHG, where we were able to obtain an amplitude increase in the reflected pulse by a factor of five without using extremely intense incident laser pulses. This was possible after we found optimal parameters for the density gradient combined with an optimal incident angle. Moreover, based on some simple assumptions, we were able to describe the distribution of transverse current in the vicinity of the SPP analytically in both cases. The obtained expressions together with the analytical expressions for electron density give us the possibility to fit the numerically obtained spectra of the back radiated pulse quite good.

## 7 Acknowledgment

This work has been supported by DFG TR18 and EU FP7 Eucard-2 projects.

## A Appendix

### A.1 Density profile from phase space distribution containing delta function

#### A.1.1 Parabolic case

In chapter 3 we started with the equation

$$x(p, t) = x_0(t) + \alpha(t)(p - p_0(t))^2, \quad (27)$$

which locally describes a curve in phase space. The distribution function of the electrons is given by

$$f(x, p, t) = \mathcal{C} \delta \left( x - x_0(t) - \alpha(t) (p - p_0(t))^2 \right), \quad (28)$$

where  $\mathcal{C}$  is a normalization constant. In order to get the expression of density we have to perform the integration in momentum space

$$n(x, t) = \int dp f(x, p, t). \quad (29)$$

By using well known integration properties of the Dirac delta function and doing some algebra we obtain the expression

$$n(x, t) = \frac{\mathcal{C}}{\sqrt{\alpha(t) (x - x_0(t))}}. \quad (30)$$



Note that this equation makes sense only for  $x > x_0$ . For  $x < x_0$  the density has to be zero in this model. This is true because the argument of delta function in (28) as the function of  $p$  vanishes only for  $x > x_0$ . In other words, there are no electrons on the left hand side of  $x_0$ . In order to calculate the constant  $\mathcal{C}$ , we initially write an equation for the number of particles in the interval  $\Delta x$  by integrating the density from  $x_0(t)$  to  $x_0(t) + \Delta x$

$$N_{\Delta x}(t) = \mathcal{C} \int_{x_0(t)}^{x_0(t)+\Delta x} \frac{dx}{\sqrt{\alpha(t)(x-x_0(t))}} = 2\mathcal{C}\sqrt{\frac{\Delta x}{\alpha(t)}}. \quad (31)$$

We solve the obtained equation for  $\mathcal{C}$  and insert it into equation (30). Finally, we obtain the expression for the electron density profile,

$$n(x, t) = \frac{1}{2} \frac{N}{\sqrt{\Delta x (x - x_0(t))}}, \quad (32)$$

where  $N$  is the number of particles contained between  $x_0(t)$  and  $x_0(t) + \Delta x$ . Note that the parameter  $\alpha$  cancels, so it does not affect the density profile.

### A.1.2 Whip case

In chapter 3 we started with the equation

$$x_p(p) = e^{\alpha p}. \quad (33)$$

which locally describes a curve in phase space. The distribution function of the electrons is given by

$$f(x, p) = \mathcal{C} \delta(x - x_p(p)). \quad (34)$$

Going along the same line as in the previous case, we obtain

$$n(x) = \mathcal{C} \int dp \delta(x - x_p(p)) = \frac{\mathcal{C}}{\alpha x}. \quad (35)$$

Obviously equation (33) can not be applied at the whole interval  $[0 : \Delta x]$  as in the parabolic case since the momentum of the electrons is limited by some amount, let say,  $p_{\text{cut}}$ . Therefore the description (33) is valid only on some interval  $[x_{\text{min}} : x_{\text{max}}]$ , where  $x_{\text{min}} = e^{-\alpha p_{\text{cut}}}$ . Strictly speaking by performing the integration in (35) we have to take  $-p_{\text{cut}}$  as a lower limit, instead of  $-\infty$ . This would not change the form of the result but the interval on which it is valid, namely for  $x > x_{\text{min}}$ . Consequently, we integrate the expression (35) from  $x_{\text{min}}$  to  $x_{\text{max}}$  in order to calculate  $\mathcal{C}$  and get

$$n(x) = \frac{N}{\ln\left(\frac{x_{\text{max}}}{x_{\text{min}}}\right)x}. \quad (36)$$

## A.2 Density profile from generalized phase space distribution

At first we are going to find an appropriate definition of the function  $\delta_a$  with

$$\lim_{a \rightarrow 0} \delta_a(x) = \delta(x). \quad (37)$$

Gaussian function would fulfill these conditions, but if we use it in order to define  $\delta_a$  we would not be able to solve the integral (29) analytically. That's why we define:

$$g_a(x) \equiv \frac{3}{4a} \left(1 - \frac{x^2}{a^2}\right),$$

$$\delta_a(x) \equiv \begin{cases} g_a(x) & \text{for } x \in [-a, a], \\ 0 & \text{otherwise.} \end{cases}$$

It is easy to check that with this definition  $\delta_a(x)$  does satisfy the condition (7).

Let us again calculate the electron density profile for the parabolic case with  $x(p) = \alpha p^2$ , which holds if the electron bunch moves slowly. We have

$$n_a(x) = \mathcal{C} \int dp \delta_a(x - \alpha p^2).$$

This integration is more complicated as compared to the simple  $\delta$ -function case. We have to be careful with integration boundaries, since  $\delta_a$  is a bounded support function. As a result we obtain:

$$n_a(x) = \begin{cases} \frac{2\mathcal{C}}{5a^3\sqrt{\alpha}} (3a^2 - 2x^2 + ax) \sqrt{x+a} & \text{for } x \in [-a, a] \\ \frac{2\mathcal{C}}{5a^3\sqrt{\alpha}} \left( (3a^2 - 2x^2) (\sqrt{x+a} - \sqrt{x-a}) \right. \\ \quad \left. + ax (\sqrt{x+a} + \sqrt{x-a}) \right) & \text{for } x > a \\ 0 & \text{for } x < -a. \end{cases}$$

It is straight forward to show that

$$\lim_{a \rightarrow 0} n_a(x) = n(x) = \begin{cases} \frac{\mathcal{C}}{\sqrt{\alpha x}}, \\ 0 \end{cases} \quad (38)$$

compare with (30). For the number of particles  $N_{a,\Delta x}$  on interval  $[-a : \Delta x]$ , that means

$$N_{a,\Delta x} = 2\mathcal{C} \sqrt{\frac{\Delta x}{\alpha}} \quad \text{for } a \ll \Delta x, \quad (39)$$

compare with (31). The equation (39) follows directly from (31) and (38) for  $a \rightarrow 0$ . Via integration of  $n_a(x)$  on the interval  $[-a, \Delta x]$  it can be shown that (39) holds also for  $a \ll \Delta x$ , which is a more general case. Actually we are always able to chose  $\Delta x$  in such a way that the condition  $a \ll \Delta x$  is satisfied

and for that case we can finally write

$$n_{a,\Delta x}(x) = \begin{cases} \frac{N_{a,\Delta x}}{5a^3\sqrt{\Delta x}} (3a^2 - 2x^2 + ax) \sqrt{x+a} & \text{for } x \in [-a, a] \\ \frac{N_{a,\Delta x}}{5a^3\sqrt{\Delta x}} \left( (3a^2 - 2x^2) (\sqrt{x+a} - \sqrt{x-a}) \right. \\ \quad \left. + ax (\sqrt{x+a} + \sqrt{x-a}) \right) & \text{for } x > a \\ 0 & \text{for } x < -a. \end{cases} \quad (40)$$

## References

- [1] T. H. Maiman, “Stimulated optical radiation in ruby”, *Nature* 187, 493–494 (1960).
- [2] Strickland, D., and G. Mourou, “Compression of amplified chirped optical pulses”, *Opt. Commun.* 56, 219–211 (1985).
- [3] M. Pessot, J. Squier, G. Mourou, and D. J. Harter, “Chirped-pulse amplification of 100-fsec pulses”, *Opt. Lett.* 14, 797–799 (1989).
- [4] M. Pessot, J. Squier, P. Bado, G. Mourou, and D. J. Harter, “Chirped pulse amplification of 300 fs pulses in an alexandrite regenerative amplifier”, *J. Quantum Electron.*, QE-25, 61 (1989).
- [5] F. G. Patterson and M. D. Perry, “Design and performance of a multi-terawatt, subpicosecond neodymium:glass laser”, *J. Opt. Soc. Am. B* 8, 2384–2391 (1991).
- [6] G. Mourou and D. Umstadter “Development and applications of compact high-intensity lasers” *Phys. Fluids B* 4, 2315 (1992).
- [7] J. P. Watteau, G. Bonand, J. Coutant, P. Dautray, A. Decoster, M. Luis-Jaquet, J. Ouvry, J. Sauteret, S. Sezuec, and D. Teychenne, “Experimental program on the 20 TW laser system”, *Phys. Fluids B* 4, 2217 (1992).
- [8] Perry, M. D., and G. Mourou, “Terawatt to petawatt subpicosecond lasers”, *Science* 264, 917–924 (1994).
- [9] Mourou, G., “The ultrahigh-peak-power laser: present and future”, *Appl. Phys. B: Lasers Opt.* 65, 205–211 (1997).
- [10] A. Baltuska, M. Uiberacker, E. Goulielmakis, R. Kienberger, V. S. Yakovlev, T. Udem, T. W. Hansch, and F. Krausz, “Phase-controlled amplification of few-cycle laser pulses”, *IEEE J. Sel. Top. Quantum Electron.* 9, 972 (2003).
- [11] Norreys, P. A., K. M. Krushelnick, and M. Zepf, “PW lasers: Matter in extreme laser fields”, *Plasma Phys. Controlled Fusion* 46, B13–B21 (2004).
- [12] S.-W. Bahk, P. Rousseau, T. A. Planchon, V. Chvykov, G. Kalintchenko, A. Maksimchuk, G. A. Mourou, and V. Yanovsky, “Generation and characterization of the highest laser intensities (1022 W/cm<sup>2</sup>)”, *Opt. Lett.* 29, 2837–2839 (2004).
- [13] Mourou, G. A., T. Tajima, and S. V. Bulanov, “Optics in the relativistic regime”, *Rev. Mod. Phys.* 78, 309–371 (2006).
- [14] V. Yanovsky, V. Chvykov, G. Kalinchenko, P. Rousseau, T. Planchon, T. Matsuoka, A. Maksimchuk, J. Nees, G. Cheriaux, G. Mourou, and K. Krushelnick, “Ultra-high intensity- 300-TW laser at 0.1 Hz repetition rate”, *Opt. Express* 16, 2109–2114 (2008).
- [15] G. A. Mourou and T. Tajima, “More Intense, Shorter Pulses”, *Science* 331, 41 (2011).

- [16] G. Mourou, S. Mironov, E. Khazanov and A. Sergeev, “Single cycle thin film compressor opening the door to Zeptosecond-Exawatt physics” *Eur. Phys. J. Special Topics* 223, 1181-1188 (2014).
- [17] Carman, R. L., D. W. Forslund, and J. M. Kindel, “Visible harmonic emission as a way of measuring profile steepening”, *Phys. Rev. Lett.* 46, 29–32 (1981).
- [18] Carman R. L., D. W. Forslund, and J. M. Kindel, “Observation of harmonics in the visible and ultraviolet created in CO<sub>2</sub>-laser produced plasmas”, *Phys. Rev. A* 24, 2649–2663 (1981).
- [19] Hentschel, M., R. Kienberger, Ch. Spielmann, G. A. Reider, N. Milosevic, T. Brabec, P. Corkum, U. Heinzmann, M. Drescher, and F. Krausz, “Attosecond metrology”, *Nature* 414, 509–513 (2001).
- [20] A. Baltuska, T. Udem, M. Uiberacker, M. Hentschel, E. Goulielmakis, C. Gohle, R. Holzwarth, V. S. Yakovlev, A. Scrinzi, T. W. Hansch, and F. Krausz, “Attosecond control of electronic processes by intense light fields”, *Nature (London)* 421, 611 (2003).
- [21] G. Sansone, E. Benedetti, F. Calegari, C. Vozzi, L. Avaldi, R. Flammini, L. Poletto, P. Villoresi, C. Altucci, R. Velotta, S. Stagira, S. De Silvestri, and M. Nisoli, “Isolated Single-Cycle Attosecond Pulses”, *Science* 314, 443 (2006).
- [22] E. Goulielmakis, M. Schultze, M. Hofstetter, V. Yakovlev, J. Gagnon, M. Uiberacker, A. L. Aquila, E. M. Gullikson, D. T. Attwood, R. Kienberger, F. Krausz, and U. Kleineberg, “Single-Cycle Nonlinear Optics”, *Science* 320, 1614 (2008).
- [23] C. Thaury, F. Quéré, J.P. Geindre, A. Levy, T. Ceccotti, P. Monot, M. Bougeard, and F. Réau, “Plasma mirrors for ultrahigh-intensity optics”, *Nature Physics* 3, 424-429 (2007).
- [24] F. Quéré, C. Thaury, P. Monot, S. Dobosz, P. Martin, J.-P. Geindre, and P. Audebert, “Coherent Wake Emission of High-Order Harmonics from Overdense Plasmas”, *Phys. Rev. Lett.* 96, 125004 (2006).
- [25] P. Heissler, R. Hörlein, M. Stafe, J. Mikhailova, Y. Nomura, D. Herrmann, R. Tautz, S. Rykovanov, I. Földes, K. Varju, F. Tavella, A. Marcinkevicius, F. Krausz, L. Veisz, and G. Tsakiris, “Toward single attosecond pulses using harmonic emission from solid-density plasmas”, *Appl. Phys. B* 101, 511 (2010).
- [26] F. Brunel, “Not-so-resonant, resonant absorption”, *Phys. Rev. Lett.* 59, 52–55 (1987).
- [27] S. V. Bulanov, N. M. Naumova, and F. Pegoraro, “Interaction of an ultra-short, relativistically strong laser pulse with an overdense plasma”, *Phys. Plasmas* 1, 745 (1994).
- [28] R. Lichters, J. M. ter Vehn, and A. Pukhov, “Short-pulse laser harmonics from oscillating plasma surface driven at relativistic intensity”, *Phys. Plasmas* 3, 3425 (1996).

- [29] D. von der Linde and K. Rzàzewski, “High-order optical harmonic generation from solid surfaces”, *Appl. Phys. B: Laser Opt.* **63**, 499 (1996).
- [30] S. Gordienko, A. Pukhov, O. Shorokhov, and T. Baeva, “Relativistic Doppler Effect: Universal Spectra and Zeptosecond Pulses”, *Phys. Rev. Lett.* **93**, 115002 (2004).
- [31] S. Gordienko, A. Pukhov, O. Shorokhov, and T. Baeva, “Coherent Focusing of High Harmonics: A New Way Towards the Extreme Intensities”, *Phys. Rev. Lett.* **94**, 101903 (2005).
- [32] T. Baeva, S. Gordienko, A. Pukhov, “Theory of high-order harmonic generation in relativistic laser interaction with overdense plasma”, *Phys. Rev. E* **74**, 046404 (2006).
- [33] B. Dromey, M. Zepf, A. Gopal, K. Lancaster, M. S. Wei, K. Krushelnick, M. Tatarakis, N. Vakakis, S. Moustazis, R. Kodama, M. Tampo, C. Stoeckl, R. Clarke, H. Habara, D. Neely, S. Karsch, and P. Norreys, “High harmonic generation in the relativistic limit”, *Nat. Phys.* **2**, 456–459 (2006).
- [34] B. Dromey, S. Kar, C. Bellei, D. C. Carroll, R. J. Clarke, J. S. Green, S. Kneip, K. Markey, S. R. Nagel, P. T. Simpson, L. Willingale, P. McKenna, D. Neely, Z. Najmudin, K. Krushelnick, P. A. Norreys, and M. Zepf, “Bright multi-keV harmonic generation from relativistically oscillating plasma surfaces”, *Phys. Rev. Lett.* **99**, 085001 (2007).
- [35] P. Heissler, R. Hörlein, J. M. Mikhailova, L. Waldecker, P. Tzallas, A. Buck, K. Schmid, C. M. S. Sears, F. Krausz, L. Veisz, M. Zepf and G. D. Tsakiris, *Phys. Rev. Lett.* **108**, 235003 (2012).
- [36] D. an der Brügge and A. Pukhov, “Enhanced relativistic harmonics by electron nanobunching”, *Phys. Plasmas* **17**, 033110 (2010).
- [37] D. an der Brügge, A. Pukhov, “Theory of Attosecond Pulses from Relativistic Surface Plasmas”, Preprint at <http://arxiv.org/abs/1111.4133v1> (2011).
- [38] B. Dromey, S. Rykovanov, M. Yeung, R. Hörlein, D. Jung, D. C. Gautier, T. Dzelzainis, D. Kiefer, S. Palaniyppan, R. Shah, J. Schreiber, H. Ruhl, J. C. Fernandez, C. L. S. Lewis, M. Zepf, and B. M. Hegelich, “Coherent synchrotron emission from electron nanobunches formed in relativistic laserplasma interactions”, *Nat. Phys.* **8**, 804–808 (2012).
- [39] B. Dromey, S. Cousens, S. Rykovanov, M. Yeung, D. Jung, D. C. Gautier, T. Dzelzainis, D. Kiefer, S. Palaniyppan, R. Shah, J. Schreiber, J. C. Fernandez, C. L. S. Lewis, M. Zepf, and B. M. Hegelich, “Coherent synchrotron emission in transmission from ultrathin relativistic laser plasmas”, *New J. Phys.* **15**, 015025 (2013).
- [40] M. Yeung, B. Dromey, S. Cousens, T. Dzelzainis, D. Kiefer, J. Schreiber, J. H. Bin, W. Ma, C. Kreuzer, J. Meyerter-Vehn, M. J. V. Streeter, P. S. Foster, S. Rykovanov, and M. Zepf, “Dependence of Laser-Driven Coherent Synchrotron Emission Efficiency on Pulse Ellipticity and Implications for Polarization Gating”, *Phys. Rev. Lett.* **112**, 123902 (2014).

- [41] A. A. Gonoskov, A. V. Korzhimanov, A. V. Kim, M. Marklund and A. M. Sergeev1, “Ultrarelativistic nanoplasmonics as a route towards extreme-intensity attosecond pulses”, *Phys. Rev. E* **84**, 046403 (2011).
- [42] S. Gordienko, A. Pukhov, “Scalings for ultrarelativistic laser plasmas and quasimonoenergetic electrons”, *Phys. Plasmas* **12**, 043109 (2005).
- [43] T Baeva, S Gordienko, A Pukhov *Physical Review E* 74 (6), 065401 (2006)
- [44] S. G. Rykovanov, M. Geissler, J. Meyer-ter-Vehn, and G. D. Tsakiris, “Intense single attosecond pulses from surface harmonics using the polarization gating technique”, *New J. Phys.* 10, 025025 (2008).
- [45] A. Pukhov, “X-rays in a flash”, *Nat. Phys.* 2, 439 (2006).
- [46] N. M. Naumova, J. A. Nees, I.V. Sokolov, B. Hou, and G. A. Mourou, “Relativistic Generation of Isolated Attosecond Pulses in a  $\lambda^3$  Focal Volume”, *Phys. Rev. Lett.* 92, 063902 (2004).
- [47] A. Pukhov, Three-dimensional electromagnetic relativistic particle-in-cell code VLPL (Virtual Laser Plasma Lab), *J. Plasma Phys.* **61**, 425 (1999).
- [48] Hui-Chun Wu, Preprint at <http://arxiv.org/abs/1104.3163>, (2011).